



HAL
open science

The Imbricated Foreshock and Aftershock Activities of the Balsorano (Italy) Mw 4.4 Normal Fault Earthquake and Implications for Earthquake Initiation

Hugo Samuel Sánchez Reyes, David Essing, Eric Beaucé, Piero Poli

► **To cite this version:**

Hugo Samuel Sánchez Reyes, David Essing, Eric Beaucé, Piero Poli. The Imbricated Foreshock and Aftershock Activities of the Balsorano (Italy) Mw 4.4 Normal Fault Earthquake and Implications for Earthquake Initiation. *Seismological Research Letters*, 2021, 92 (3), pp.1926-1936. 10.1785/0220200253 . hal-03197363

HAL Id: hal-03197363

<https://hal.univ-grenoble-alpes.fr/hal-03197363v1>

Submitted on 13 Apr 2021

HAL is a multi-disciplinary open access archive for the deposit and dissemination of scientific research documents, whether they are published or not. The documents may come from teaching and research institutions in France or abroad, or from public or private research centers.

L'archive ouverte pluridisciplinaire **HAL**, est destinée au dépôt et à la diffusion de documents scientifiques de niveau recherche, publiés ou non, émanant des établissements d'enseignement et de recherche français ou étrangers, des laboratoires publics ou privés.

1 The imbricated foreshock and aftershock activities of
2 the Balsorano (Italy) M_w 4.4 normal fault earthquake
3 and implications for earthquake initiation

4 H. S. Sánchez-Reyes¹, D. Essing¹, E. Beaucé², P. Poli¹

5 ¹*Institute of Earth Sciences, University Grenoble Alpes, Grenoble 38100, France*

6 ²*Department of Earth, Atmospheric, and Planetary Sciences, Massachusetts Institute of*
7 *Technology, Cambridge, MA, United States*

8 * *Corresponding author: hugo.sanchez-reyes@univ-grenoble-alpes.fr*

9 **Key words:**

10 • earthquake initiation process

11 • earthquake sequence

12 • spatio-temporal evolution

13 **Key points:**

14 • The analysis of the 2019 Balsorano earthquake sequence reveals that imbricated com-
15 plex processes occur before and after the main earthquake

16 • Clear differences between foreshocks and aftershocks are highlighted by the distinct
17 spatio-temporal patterns unraveled by our analysis

18 • These results demonstrate that simple earthquake preparation models are not suitable
19 enough to correctly mimic the observed complex reality

Abstract

Foreshocks in the form of microseismicity are among the most powerful tools to study the physical processes that occur before main earthquakes. However, their detection and precise characterization is still sparse, especially for small to moderate-sized earthquakes ($M_w < 6$). We present here a detailed foreshock analysis for the November 7, 2019, Balsorano (Italy) normal fault earthquake (M_w 4.4). To improve the detection of the microseismicity before and after the mainshock, we use six three-component broadband receivers at distances of less than 75 km from the targeted seismicity, through template matching. To improve the understanding of the physical mechanism(s) behind the earthquake initiation process, as well as other accompanying phenomena, we also detail the spatio-temporal evolution of the sequence associated to this medium-sized earthquake, using waveform clustering and hypocenter relocation. Clear differences between foreshocks and aftershocks are revealed by this analysis. Moreover, five distinct spatio-temporal patterns associated to the different seismic activities are revealed. The observed spatio-temporal behavior shown by the foreshocks highlights a complex initiation process, which apparently starts on an adjacent unmapped antithetic fault. Finally, the aftershock activity comprises four different clusters with distinct spatio-temporal patterns, which suggests that the different clusters in this sequence have distinct triggering mechanisms.

Introduction

The detection of signals that can inform us about a forthcoming earthquake is fundamental to build physical models that mimic the processes behind the triggering and nucleation of earthquakes. These physical models are important because they provide us the basis to characterize earthquakes. Therefore, the study and analysis of precursory signals are of great importance. Over the last 25 years, numerous studies have reported a wide range of observations that appear to be connected with the physics that precedes large seismic events

46 (*e.g.* [Rikitake, 1975](#); [Jones and Molnar, 1979](#); [Molchanov et al., 1998](#); [Eftaxias et al., 2000](#);
47 [Virk and Walia, 2001](#); [Singh et al., 2010](#); [De Santis et al., 2019](#); [Jones, 1985](#); [Abercrombie
48 and Mori, 1996](#); [Felzer et al., 2004](#); [Dodge et al., 1996](#); [Ellsworth and Bulut, 2018](#); [Yoon
49 et al., 2019](#); [Reasenber, 1999](#); [Ruiz et al., 2017, 2014a](#)). Among these, some of the most
50 compelling are the ones based on seismological characterization of foreshock sequences,
51 as well as other seismological observations and their relationships with mainshocks (*e.g.*
52 [Jones, 1985](#); [Abercrombie and Mori, 1996](#); [Reasenber, 1999](#); [Felzer et al., 2004](#); [Dodge
53 et al., 1996](#); [Bouchon et al., 2011](#); [Ruiz et al., 2014b, 2017](#); [Ellsworth and Bulut, 2018](#); [Yoon
54 et al., 2019](#)). Foreshocks are thus one of the most useful tools to understand the physics of
55 earthquake initiation in real faults ([Brune, 1979](#); [Abercrombie and Mori, 1996](#); [Malin et al.,
56 2018](#)). Therefore, it is important to improve foreshock observations and characterization,
57 particularly for the more frequent small to moderate-sized events (*i.e.* $M_w < 6$), as these
58 might share similar physical processes with larger events. These improved observations
59 may shed light on the physical processes that occur during the triggering and nucleation of
60 earthquakes and will drive future research that focuses on theoretical and numerical models
61 to better characterize earthquake occurrence in real and complex faults.

62 Earthquake initiation (*e.g.* [Kato et al., 2012](#); [Schurr et al., 2014](#); [Tramutoli et al., 2015](#))
63 and earthquake nucleation/triggering (*e.g.* [Dieterich, 1992](#); [Ellsworth and Beroza, 1995](#);
64 [Rubin and Ampuero, 2005](#)) are two different, and perhaps overlapping, phases of the seismic
65 cycle. While the first is understood to occur over the longer term preceding a large event
66 (*i.e.*, days or months, to years), the second occurs some minutes to seconds before the main
67 event. Both phases, however, can be explained under the Dieterich model ([1994](#)), which
68 relates the seismicity rate to the stressing history through a rate-and-state constitutive law.
69 For earthquake initiation in particular for real faults, two main hypotheses are currently
70 used to explain this process. Some authors argue that a mainshock is a consequence of a
71 cascade process, with stress transfer in-between events, which eventually trigger the large
72 event (*e.g.*, [Dodge et al., 1996](#); [Ellsworth and Bulut, 2018](#); [Yoon et al., 2019](#)). Alternatively,

73 the initiation of an earthquake can be understood as an aseismic process that weakens the
74 pre-existing asperities, until a larger rupture is promoted (Dodge et al., 1996; Bouchon
75 et al., 2011; Tape et al., 2018). In the latter case, foreshocks result from the activation
76 of brittle asperities by the surrounding aseismic slip processes. However, intermediate
77 models that involve both triggering and aseismic slip are likely for complex faults (*e.g.*
78 McLaskey, 2019). This complexity might result from fault heterogeneity (*e.g.*, variable
79 stress, frictional properties) and promote imbricated sequences of foreshocks and aseismic
80 slip (*e.g.*, Dublanchet, 2018).

81 The monitoring of foreshocks is today routine in laboratory experiments (Zang et al.,
82 1998; Goebel et al., 2012; Renard et al., 2019, and references therein), while studies that
83 focus on large earthquakes remain relatively sparse (*i.e.*, $M_w > 6$) (*e.g.*, Mogi, 1963; Aber-
84 crombie and Mori, 1996; Kato et al., 2012; Chen and Shearer, 2013; Bouchon et al., 2013;
85 Ruiz et al., 2014b). However, the recent improvements to seismological monitoring systems
86 around active faults have now provided detailed analysis of foreshocks that precede the
87 more frequent small to moderate-sized earthquakes ($M_w < 6$) (*e.g.*, Savage et al., 2017;
88 McMahon et al., 2017; Malin et al., 2018). One intriguing feature that has emerged from
89 these more recent studies is the increased complexity (*i.e.*, fault interactions, volumetric
90 processes) that have been revealed through the availability of better data (*e.g.*, near-fault
91 receivers) and more advanced detection methods (*e.g.*, template matching) to study fore-
92 shocks. This complexity might challenge the actual laboratory scale and theoretical models,
93 which treat earthquake initiation as simple physical processes that occur in smooth fault
94 planes (Dieterich, 1992; Marone, 1998; Rubin and Ampuero, 2005; Liu and Rice, 2005).
95 The necessity for high-resolution characterization of foreshocks based on good data and
96 advanced data processing techniques was also suggested by a meta-analysis carried out by
97 Mignan (2014), which indicated resolution-dependent bias for earthquake initiation models
98 that were resolved using seismological data.

99 To shed new light on the physical processes that occur before relatively small earth-

100 quakes, we study here the medium-sized (M_w 4.4) Balsorano normal fault earthquake and
101 its foreshock-aftershock sequence (Fig. 1). The Italian National Institute of Geophysics and
102 Volcanology (*Istituto Nazionale di Geofisica e Vulcanologia*; INGV; [online catalog](#)) reported
103 that the main event of this sequence occurred on November 7, 2019 (17:35:21.18 UTC), ap-
104 proximately 4 km southeast of Balsorano city in central Italy (Fig. 1). The hypocenter
105 of this main event was located relatively deep in the crust (14 km), close to the transition
106 zone between the upper and lower crust (10-20 km in depth), where the brittle locked fault
107 transitions into the ductile regime zone ([Doglioni et al., 2011](#)). Below this depth, the lower
108 crust is relatively seismically silent ([Doglioni et al., 2011](#)). According to a geological study
109 ([Roberts and Michetti, 2004](#)), the surface morphology presented by [Falcucci et al. \(2016\)](#)
110 and [Wedmore et al. \(2017\)](#), together with the main event location and its focal mechanism
111 (Supplementary Material Table S1), we assume that this event ruptured a segment of the
112 Liri fault, which is one of the major active normal faults mapped in this region. This struc-
113 ture accommodates the low extension rate observed in this region (*i.e.*, a few millimeters
114 per year) ([Hunstad and England, 1999](#); [Westaway, 1992](#); [D’agostino et al., 2001](#); [Roberts](#)
115 [and Michetti, 2004](#)). However, we recognize that this assumed geometry (based on the
116 estimated focal mechanism) might be biased, and that the inclusion of body waves into the
117 moment tensor solution (*e.g.* [Zhao and Helmberger, 1994](#); [Zhu and Helmberger, 1996](#), *CAP*
118 *method*) should improve such estimation.

119

[Figure 1]

120 In addition to the mainshock of November 7, 2019, 135 events occurred close to the
121 epicenter of the main event from October 22 to November 15, 2019 (which included 25
122 foreshocks). Starting from these cataloged events, we study here the ‘anatomy’ of the
123 foreshocks and aftershocks, and their relationships with the main event. With this aim,
124 continuous data from six three-component stations at less than 75 km from the mainshock
125 epicenter are used (Fig. 1; Supplementary Materials Table S2). The continuous waveforms

126 recorded are analyzed using template matching techniques (Gibbons and Ringdal, 2006;
127 Shelly et al., 2007) to detect smaller events and thus to expand upon the available seismic
128 catalog. The detected events are then relocated using the double-difference method (Wald-
129 hauser, 2001), to reveal the geometry of the main fault and to obtain new insights into
130 the fault-slip behavior(s) before and after the main seismic event. Furthermore, through
131 waveform clustering, we isolate families of earthquakes that are representative of different
132 physical processes that occur in the pre- and post-mainshock period. This combination of
133 detection, relocation, and waveform clustering reveals an imbricated seismic sequence where
134 several faults were activated, and with clear differences in the spatio-temporal properties
135 of the foreshocks and aftershocks.

136 Methods

137 **Template matching:** The analysis starts by extending the INGV seismic catalog using the
138 template matching approach (Gibbons and Ringdal, 2006). From the 135 events reported
139 by the INGV online catalog , where 25 events are identified as foreshocks, we retain only
140 the events with available P-wave and S-wave picks for all of the six stations used. We then
141 extract 4 s of signal, starting 1 s before the phase arrival time from the band-pass filtered
142 data (5-20 Hz). Using the pre-picked signals, we estimate the signal-to-noise ratio and
143 retain as templates only those events with a signal-to-noise ratio >3 at all of the stations.
144 With this data selection, 23 events are obtained (including three foreshocks) that are the
145 templates used for scanning the continuous data (Supplementary Materials Table S4). We
146 use three-component data with P waves extracted from the vertical component, and S waves
147 extracted from the East and North components.

148 In all, 28 days of continuous data are processed, from October 22 (*i.e.*, 16 days before
149 the mainshock) to November 15, 2019, using the fast matched filter algorithm from Beaucé
150 et al. (2017). The detection thresholds are set to 12 times the daily median absolute devi-

151 ation of the summed correlation coefficients over the array of stations. Finally, consecutive
152 detections with differential times of <3 s are removed (*i.e.*, the time difference between two
153 estimated origin times).

154 The final catalog contains 714 events (166 foreshocks, 547 aftershocks), which represents
155 ~ 6 -fold the number of events in the initial catalog. To estimate the magnitudes of the
156 newly detected events, we use the average root mean square in the time window containing
157 the S waves over all of the stations and components. Least-square fitting is then used
158 to obtain a linear model that relates the logarithmic of the root mean square of the 23
159 templates and their local magnitudes from the INGV catalog. This model is then used to
160 estimate the magnitude of the newly detected events. A summary of the event occurrences
161 in time together with their magnitudes is shown in Figure 2.

162 [Figure 2]

163 **Waveform-based clustering:** Clustering is widely used in seismology to recognize
164 patterns in spatio-temporal events, which include the identification of foreshock-aftershock
165 sequences and stress evolution in time (*e.g.*, [Kagan and Jackson, 1991](#); [Wehling-Benatelli
166 et al., 2013](#); [Cesca et al., 2014](#); [Ellsworth and Bulut, 2018](#)). Here, we apply a hierarchi-
167 cal clustering analysis ([Ward Jr, 1963](#)) to define groups of events inside the earthquake
168 sequence. The dissimilarity between the waveforms of the events in the sequence is used
169 as the distance metric for this clustering analysis. For this analysis, we estimate the dis-
170 similarity (D) between two events, i and j , as $D_{i,j} = 1 - C_{i,j}$ being C_{ij} the correlation
171 coefficient associated to that pair of events. For this, the full normalized waveforms are
172 used to calculate the correlation coefficient, with a 4.5-s time window (starting 0.5 s be-
173 fore the P-wave arrival) that contains both the P phase and the S phase. Under these
174 assumptions, it is important to stress out that the events composing a defined group by the
175 hierarchical clustering analysis do not necessarily share similar locations and/or a common
176 rupture mechanism.

177 The waveforms of the 714 detected events recorded at the closest station to the epicenter
178 (Fig. 1, VVLD) are then correlated with each other. The correlation matrix obtained (Fig.
179 3a) is used to estimate the distance (dissimilarity) metric to perform hierarchical clustering.
180 The Ward minimum variance method is used (Ward Jr, 1963) with a distance threshold
181 of 5.5 defined (Supplementary Materials Fig. S1: the largest separation observed from the
182 dendrogram). This hierarchical clustering analysis highlights five different groups (clusters),
183 as shown in Figure 3b, c. As both the P waves and S waves are used for clustering, the
184 resulting family members might share, but not necessarily, similarities in position and
185 rupture mechanism (Kagan and Jackson, 1991; Wehling-Benatelli et al., 2013; Cesca et al.,
186 2014; Ellsworth and Bulut, 2018; Cattaneo et al., 1999).

187 **Relocation:** We finally estimate the relative location between the detected events using
188 the double-difference algorithm (HypoDD software; Waldhauser (2001)). The differential
189 times of the P phases and S phases between events from the cross-correlation are estimated,
190 with the retention of only the delays that are associated to correlation coefficients >0.6 .
191 We further limit the delays to 0.2 s. After discarding the event pairs that relate less than
192 3 P-wave and 3 S-wave highly correlated differential times (correlation coefficient, ≥ 0.6),
193 the final number of 29859 pairs are kept and used in the relocation process.

194 For each newly detected event, we assume its initial location as the coordinates of the
195 template that reports the highest correlation coefficient related to that event. In addition,
196 we assume the estimated P-wave and S-wave picks obtained from our template matching
197 analysis as the initial catalog information for the relocation. A velocity model for this region
198 proposed by Bagh et al. (2007) is used in the relocation process (Supplementary Materials
199 Table S3). Following previous studies (Shelly and Hardebeck, 2019), the inversion is per-
200 formed with stronger weights to the initial information related to the P-wave and S-wave
201 picks from the catalog (*i.e.*, from the template matching analysis), while the differential
202 times from the waveform correlations control the final iterations. In the end, 689 of the
203 714 newly detected events are successfully relocated. The temporal and geometric patterns

204 observed in this earthquake sequence are illustrated in Figures 4 and 5, and are further
205 described in the following section.

206 [Figure 3]

207 **Results and discussion**

208 The time evolution of the detected events is shown in Figure 2. Of the 714 events, 166 are
209 foreshocks (23%). Together with the temporal evolution, Figure 2a shows the spectrogram
210 and the average spectral energy in a frequency band from 5 Hz to 20 Hz. The oscillation
211 of this energy suggests variable noise levels in the study area, with lower noise during the
212 night (Figure 2, shaded areas, for periods from 18:00 to 06:00). This noise variation is
213 related to anthropogenic activity (Poli et al., 2020b), and it is also observed for the other
214 five receivers. This noise evolution will probably affect our detection performance. For
215 example, it is not clear if the reduced number of events observed prior to the mainshock is
216 real or is a consequence of the higher noise level (Fig. 2b). We thus avoid discussing any
217 issue related to pre-seismic quiescence here. However, with the geometric and clustering
218 information derived above, we can still characterize some of the properties of the newly
219 detected foreshocks and aftershocks, and gain insight into the physical processes that occur
220 at the different stages of the sequence.

221 The results from the combination of waveform clustering and relocation strategies are
222 summarized in Figures 4 and 5. For each cluster, the coefficient of variation (COV) is also
223 estimated from the recurrence time of the events (Kagan and Jackson, 1991; Schoenball
224 and Ellsworth, 2017). The COV indicates the level of the temporal clustering within each
225 group (*i.e.*, how much the occurrence of future earthquakes depends on the occurrence of the
226 past earthquakes): with $COV=1$ for random seismicity, and $COV>1$ for strong temporal
227 clustering. The larger the COV, the more the earthquakes are interacting. Thus, it is

228 important to note that events that happen together with a high COV mean that there is
229 an intrinsically related interaction between them.

230 The temporal and spatial densities of the different clusters identified in this sequence
231 are illustrated in Figure 4, where cluster 1 (green solid lines and dots) is mainly composed
232 of foreshocks (161 of 209 events occurred before the mainshock). The events that form this
233 family show the highest waveform similarity (Fig. 3a). In agreement with this waveform
234 property, cluster 1 has high spatial density, with approximately 90% of its activity (193
235 of the 208 events) located within 0.5 km of the mainshock hypocenter (Figs. 4a and 5a).
236 Cluster 1 also shows the highest temporal clustering (COV=4.8; Fig. 4a).

237 The next two families, as cluster 2 (COV=3.0; Figure 4b, blue solid lines and dots)
238 and cluster 3 (COV=2.9; Figure 4c, magenta solid lines and dots), share similar temporal
239 clustering values, but show differences with respect to their spatial densities. While ap-
240 proximately 90% of the events of cluster 2 are within 0.8 km of the hypocenter (136 of 151
241 events; Fig. 4b), cluster 3 has almost 90% of its activity (187 of 211 events) located over
242 a larger volume, as approximately 1.2 km from the mainshock location (Fig. 4c). Cluster
243 4 (Figure 4d, brown solid lines and dots) is characterized by 90% of its activity within 0.6
244 km of the mainshock hypocenter (53 of 59 shocks; Fig. 4d). The seismicity in this cluster
245 is also characterized by high temporal clustering (COV=4.2). Cluster 5 (COV=2.2; Figure
246 4e, red solid lines and dots) is the least temporally clustered, but with the second highest
247 spatial density (after cluster 1), with 90% of its activity in a region 0.5 km from the main-
248 shock hypocenter (66 of 73 events; Fig. 4e). A general spatial pattern of this sequence is
249 the concentration of events close to the mainshock that occurred prior to it (110 foreshocks
250 within 0.3 km) and the subsequent spread over a region >0.3 km during the aftershocks.

251 Figure 5 illustrates the geometric patterns related to each of the clusters, as defined
252 by the relocation process. A remarkable pattern can be seen in Figure 5a: cluster 1 (*i.e.*,
253 foreshocks) shows an antithetical orientation with respect to the assumed fault plane of
254 the main event (Fig. 5a, map view and cross sections). In contrast, clusters 4 and 5 show

255 nearly parallel orientations with respect to the assumed main fault plane (Fig. 5d, e, cross-
256 sections, respectively). We also observe particular behavior for cluster 5, which is the only
257 cluster where the activity is exclusively to the northeast of the mainshock hypocenter and
258 on the footwall (Fig. 5e, map view and cross-sections). The events in cluster 5 follow an
259 orientation that is parallel to the assumed main fault plane dipping angle (Fig. 5e, cross-
260 section). In turn, cluster 3 has an activity that follows the orientation of the fault plane, but
261 that spreads across the whole volume surrounding the fault plane (Fig. 5c, cross-sections).

262 [Figure 4]

263 [Figure 5]

264 The results of the spatio-temporal evolution for the identified clusters suggest complex
265 evolution of the seismicity. Two fault planes are activated during the sequence, with fore-
266 shocks primarily occurring on the antithetic fault plane (Fig. 5a, cross-section), similarly to
267 part of the foreshock activity that was observed for the L'Aquila normal fault earthquake
268 (Chiaraluce et al., 2011). Relying only on our observations, it is hard to unravel which
269 mechanism(s) might be responsible for the occurrence of the foreshocks, and thus the driv-
270 ing of the main event. For example, there are no exponential or power-law increments
271 of events seen while approaching the main event (Papazachos, 1975; Kagan and Knopoff,
272 1978), which might suggest accelerating aseismic slip (Dodge et al., 1996; Bouchon et al.,
273 2011; Tape et al., 2018). Neither are any spatial patterns seen (*e.g.*, migrations) that might
274 suggest the same mechanism, or might alternatively indicate triggering by stress transfer
275 (Dodge et al., 1996; Ellsworth and Bulut, 2018; Yoon et al., 2019). However, we clearly
276 outline the differences between the foreshocks and aftershocks. In particular, the fore-
277 shocks occur in a more temporal clustered manner, and they are closer to the hypocenter
278 of the main event (Fig. 4a). The compact and highly temporal clustered seismicity indi-
279 cates strong event interactions, and favors stress transfer as the mechanism for foreshock
280 occurrence (COV, Schoenball and Ellsworth, 2017).

281 In order to investigate if aseismic slip triggered, to some extent, the mainshock, we search
282 for seismological evidences such as the existence of repeating earthquakes in the foreshock
283 sequence (Uchida, 2019). The resulting waveform-based correlation matrix (Fig. 3a) shows
284 118 pairs with correlation coefficients larger than 0.95 (61 pairs of foreshocks and 57 pairs
285 of aftershocks). Regarding the estimated relocation of those highly correlated foreshock
286 waveform pairs, 44 out of the 61 pairs (72%) show a practically overlapping location (relative
287 distances < 20 m) considering the uncertainty of the relocation (approximately 20 m).
288 However, the significantly low magnitudes (123 out of 166 foreshocks have magnitudes
289 smaller than 0.5) and the limited frequency range used in our analysis (5-20 Hz) do not
290 allow us to properly conclude about the existence of repeaters in this sequence (Uchida,
291 2019; Uchida and Bürgmann, 2019).

292 Interestingly, the aftershock clusters also show different spatio-temporal behaviors be-
293 tween each other (Figs. 5b-e, 4b-e). The observed differences might be explained by
294 different physical processes driving the aftershock occurrence. For example, clusters 2 and
295 3 (Fig. 5b, c) spread in a wide volume around the fault in contrast to the other clusters.
296 This spatial pattern is likely to result from stress redistribution, volumetric damage, and
297 relaxation processes after the mainshock (Trugman et al., 2020). In particular, the spatio-
298 temporal evolution of the zone containing cluster 3 expands away from the hypocenter with
299 the logarithm of time (Fig. S6, Supplementary Material). The spatial expansion of the
300 active zone of cluster 3 is also evidenced by the relative small amplitude of the stacked
301 waveform estimated for cluster 3 (Fig. 3c). This feature from cluster 3 might suggest af-
302 terslip as its driving mechanism (Ross et al., 2017). Such observation might support the
303 alternative model proposed by Inbal et al. (2017), where the afterslip from the mainshock
304 might be the triggering mechanism of the aftershocks off of the main fault. Clusters 4 and
305 5 in turn are localized in a more compact volume around the assumed fault plane (Fig.
306 5d, e). This behavior suggests that the activity from these clusters result from a localized
307 stress increment close to the fault plane.

308 We also search for evidences of repeating earthquakes in the aftershock sequence. Such
309 repeaters may suggest the existence of co-planar afterslip (Nadeau and McEvilly, 1999;
310 Igarashi, 2010; Igarashi et al., 2003). Out of the 57 pairs of highly correlated aftershocks
311 (from the correlation coefficient matrix), 28 show an estimated overlapping location (relative
312 distances < 20 m). However, as mentioned above, the limited frequency range used and
313 the estimated small magnitudes of the newly detected events do not allow us to conclude
314 if co-planar afterslip might be the triggering mechanism behind some of these aftershocks.

315 As in previous studies (McMahon et al., 2017; Savage et al., 2017; McMahon et al., 2019),
316 we can see that this detailed analysis of seismic data reveals a complex and imbricated
317 earthquake sequence, for which the mainshock initiation is unlikely to result from only the
318 evolution of physical properties (*e.g.*, stress, friction) on the main fault plane. Indeed the
319 sequence begins through an interaction between the antithetic and main faults during the
320 foreshock-mainshock sequences, similar to that observed for other events (Chiaraluce et al.,
321 2011; McMahon et al., 2019). In normal faults, this behavior can be related to preseismic
322 processes in the dilation wedge located in the hanging wall (Doglioni et al., 2011). The
323 complexity of the sequence might also emerge from fluid involvement, which is known to
324 have a significant role in the control of seismicity and its 'style' in the central Apennines
325 (Antonioli et al., 2005; Poli et al., 2020a). The stress perturbations in the antithetic fault
326 might have modified the local pore pressures, with fluid migration into the main fault,
327 which would favor the occurrence of the main event (Doglioni et al., 2011).

328 Conclusion

329 By using a combination of high-resolution detection methods, precise relocation (*e.g.*, Gib-
330 bons and Ringdal, 2006; Waldhauser, 2001) and waveform clustering, we have unveiled
331 the complexity of the sequences associated with the 2019 (M_w 4.4) Balsorano earthquake.
332 We detect 714 events that comprise this sequence. These events are classified into five

333 different seismic clusters. The differences between these clusters are highlighted by their
334 distinct spatio-temporal properties that are unveiled by the waveform-based clustering anal-
335 ysis (Kagan and Jackson, 1991; Wehling-Benatelli et al., 2013; Cesca et al., 2014; Ellsworth
336 and Bulut, 2018), and by their relative source locations (Waldhauser, 2001).

337 Our results highlight different behaviors between foreshocks and aftershocks. For exam-
338 ple, foreshocks occur in a compact region near the mainshock hypocenter, and show high
339 temporal clustering (Fig. 4a). As mentioned before, no conclusive evidence of repeating
340 earthquakes in the foreshock sequence could be obtained with the data at hand. In addition,
341 strong temporal clustering and inter-event proximity between foreshocks is observed, which
342 might indicate that stress transfer triggering has the main role in driving the occurrence
343 of the foreshocks (Dodge et al., 1996). Nevertheless, there are no observations that can
344 exclude aseismic slip. The foreshock activity mainly take place in an antithetic fault (Fig.
345 5a), which suggests that the initiation processes do not only occur on one fault plane, but
346 involve larger volumes (Savage et al., 2017). This precursory antithetic activation has been
347 observed in other normal fault events (Chiaraluce et al., 2011) and it can be expected in
348 some gravity-driven normal fault models (Doglioni et al., 2011).

349 Furthermore, our analysis shows diversity for the aftershocks behavior. Indeed, four
350 different clusters comprise the aftershock sequences. Cluster 2 is spread in a volume around
351 the main fault (Fig. 5b), and might result from stress redistribution after the mainshock
352 (*e.g.*, caused by volumetric damage and the relaxation processes; Trugman et al. (2020)).
353 Cluster 3 exhibits a logarithmic spatial expansion (Fig. S6, Supplementary Material),
354 which suggests afterslip as its driving mechanism (Ross et al., 2017). According to the
355 rapid temporal decay of their activity, their compactness and spatial orientation, clusters 4
356 and 5 appear to be driven by rapid stress increments induced by the mainshock and afterslip
357 that occur near the fault plane in the few days after the mainshock (Stein and Lisowski,
358 1983; Shen et al., 1994).

359 In summary, this study of foreshocks and aftershocks highlights that simple preparation

360 models with evolution of stress and friction on a single fault plane are not suited to precisely
361 explain the evolution of the seismicity we observe here for a real fault. A relatively large
362 volume appears to be involved in the earthquake initiation, over a short time scale (~ 1 day).
363 We further highlight how the full range of aftershocks is likely to be an ensemble average
364 view of different processes, which will include afterslip, volumetric damage, and relaxation.
365 Continuing to provide detailed information about foreshocks and their relationships to the
366 mainshock and aftershocks also for relatively small events can help us to develop new and
367 more realistic models that can provide better fitting of seismological observations and shed
368 new light on the initiation of earthquakes in real faults.

369 **Data and resources**

370 The continuous seismic data used in this study are available at the Istituto Nazionale di Ge-
371 ofisica e Vulcanologia (INGV) seismological data center (http://cnt.rm.ingv.it/webservices_and_software/;
372 last accessed, March 2020) and were downloaded using obspyDMT ([https://github.com/kasra-](https://github.com/kasra-hosseini/obsipyDMT)
373 [hosseini/obsipyDMT](https://github.com/kasra-hosseini/obsipyDMT), Hosseini and Sigloch (2017)). The fast matched filter (Beaucé et al.,
374 2017) used in this study can be found at https://github.com/beridel/fast_matched_filter.
375 Some plots were made using the Generic Mapping Tools version 6.0 and PyGMT (<https://www.pygmt.org/>
376 [Wessel et al. \(2019\)](https://www.pygmt.org/)). The event clustering was performed using Scikit-learn ([https://scikit-](https://scikit-learn.org/stable/)
377 [learn.org/stable/](https://scikit-learn.org/stable/); Pedregosa et al. (2011)). Supplemental Material for this article includes
378 a PDF file containing five tables and seven figures expanding the information presented in
379 this manuscript as well as MAT file with the whole earthquake catalog obtained from this
380 study.

Acknowledgments

This research received funding from the European Research Council (ERC) under the European Union Horizon 2020 Research and Innovation Programme (grant agreement 802777-MONIFaults). Computations were performed using the University of Grenoble Alpes (UGA) High-Performance Computing infrastructures CIMENT (<https://ciment.univ-grenoble-alpes.fr>). We would like to thank the two anonymous reviewers which comments help to improve this manuscript. Finally, we thank Leoncio Cabrera and the Remote Online Sessions for Emerging Seismologists (ROSES) of the American Geophysical Union Seismology Section, whose help was very useful in the construction of some figures.

References

- Abercrombie, R. E. and Mori, J. (1996). Occurrence patterns of foreshocks to large earthquakes in the western united states. *Nature*, 381(6580):303–307.
- Antonioli, A., Piccinini, D., Chiaraluce, L., and Cocco, M. (2005). Fluid flow and seismicity pattern: Evidence from the 1997 umbria-marche (central italy) seismic sequence. *Geophysical Research Letters*, 32(10).
- Bagh, S., Chiaraluce, L., De Gori, P., Moretti, M., Govoni, A., Chiarabba, C., Di Bartolomeo, P., and Romanelli, M. (2007). Background seismicity in the central apennines of italy: The abruzzo region case study. *Tectonophysics*, 444(1-4):80–92.
- Beaucé, E., Frank, W. B., and Romanenko, A. (2017). Fast matched filter (fmf): An efficient seismic matched-filter search for both cpu and gpu architectures. *Seismological Research Letters*, 89(1):165.

- 403 Bouchon, M., Durand, V., Marsan, D., Karabulut, H., and Schmittbuhl, J. (2013). The long
404 precursory phase of most large interplate earthquakes. *Nature geoscience*, 6(4):299–302.
- 405 Bouchon, M., Karabulut, H., Aktar, M., Özalaybey, S., Schmittbuhl, J., and Bouin, M.-P.
406 (2011). Extended nucleation of the 1999 mw 7.6 izmit earthquake. *science*, 331(6019):877–
407 880.
- 408 Brune, J. N. (1979). Implications of earthquake triggering and rupture propagation for
409 earthquake prediction based on premonitory phenomena. *Journal of Geophysical Re-*
410 *search: Solid Earth*, 84(B5):2195–2198.
- 411 Cattaneo, M., Augliera, P., Spallarossa, D., and Lanza, V. (1999). A waveform similarity
412 approach to investigate seismicity patterns. *Natural hazards*, 19(2-3):123–138.
- 413 Cesca, S., Şen, A. T., and Dahm, T. (2014). Seismicity monitoring by cluster analysis of
414 moment tensors. *Geophysical Journal International*, 196(3):1813–1826.
- 415 Chen, X. and Shearer, P. M. (2013). California foreshock sequences suggest aseismic trig-
416 gering process. *Geophysical Research Letters*, 40(11):2602–2607.
- 417 Chiaraluce, L., Valoroso, L., Piccinini, D., Di Stefano, R., and De Gori, P. (2011). The
418 anatomy of the 2009 l’aquila normal fault system (central italy) imaged by high resolu-
419 tion foreshock and aftershock locations. *Journal of Geophysical Research: Solid Earth*,
420 116(B12).
- 421 D’agostino, N., Giuliani, R., Mattone, M., and Bonci, L. (2001). Active crustal extension in
422 the central apennines (italy) inferred from gps measurements in the interval 1994–1999.
423 *Geophysical Research Letters*, 28(10):2121–2124.
- 424 De Santis, A., Marchetti, D., Pavón-Carrasco, F. J., Cianchini, G., Perrone, L., Abbattista,
425 C., Alfonsi, L., Amoroso, L., Campuzano, S. A., Carbone, M., et al. (2019). Precursory

426 worldwide signatures of earthquake occurrences on swarm satellite data. *Scientific reports*,
427 9(1):1–13.

428 Dieterich, J. (1994). A constitutive law for rate of earthquake production and its application
429 to earthquake clustering. *Journal of Geophysical Research: Solid Earth*, 99(B2):2601–
430 2618.

431 Dieterich, J. H. (1992). Earthquake nucleation on faults with rate-and state-dependent
432 strength. *Tectonophysics*, 211(1-4):115–134.

433 Dodge, D. A., Beroza, G. C., and Ellsworth, W. (1996). Detailed observations of califor-
434 nia foreshock sequences: Implications for the earthquake initiation process. *Journal of*
435 *Geophysical Research: Solid Earth*, 101(B10):22371–22392.

436 Doglioni, C., Barba, S., Carminati, E., and Riguzzi, F. (2011). Role of the brittle–ductile
437 transition on fault activation. *Physics of the Earth and Planetary Interiors*, 184(3-4):160–
438 171.

439 Dublanchet, P. (2018). The dynamics of earthquake precursors controlled by effective fric-
440 tion. *Geophysical Journal International*, 212(2):853–871.

441 Eftaxias, K., Kopanas, J., Bogris, N., KAPIRIS, P., ANTONOPOULOS, G., and VAROT-
442 SOS, P. (2000). Detection of electromagnetic earthquake precursory signals in greece.
443 *Proceedings of the Japan Academy, Series B*, 76(4):45–50.

444 Ellsworth, W. L. and Beroza, G. C. (1995). Seismic evidence for an earthquake nucleation
445 phase. *Science*, 268(5212):851–855.

446 Ellsworth, W. L. and Bulut, F. (2018). Nucleation of the 1999 izmit earthquake by a
447 triggered cascade of foreshocks. *Nature Geoscience*, 11(7):531–535.

- 448 Falcucci, E., Gori, S., Galadini, F., Fubelli, G., Moro, M., and Saroli, M. (2016). Active
449 faults in the epicentral and mesoseismal ml 6.0 24, 2016 amatrice earthquake region,
450 central Italy. methodological and seismotectonic issues. *Annals of geophysics*, 59.
- 451 Felzer, K. R., Abercrombie, R. E., and Ekstrom, G. (2004). A common origin for af-
452 tershocks, foreshocks, and multiplets. *Bulletin of the Seismological Society of America*,
453 94(1):88–98.
- 454 Gibbons, S. J. and Ringdal, F. (2006). The detection of low magnitude seismic events using
455 array-based waveform correlation. *Geophysical Journal International*, 165(1):149–166.
- 456 Goebel, T., Becker, T., Schorlemmer, D., Stanchits, S., Sammis, C., Rybacki, E., and
457 Dresen, G. (2012). Identifying fault heterogeneity through mapping spatial anomalies in
458 acoustic emission statistics. *Journal of Geophysical Research: Solid Earth*, 117(B3).
- 459 Hosseini, K. and Sigloch, K. (2017). Obspydmt: a python toolbox for retrieving and pro-
460 cessing large seismological data sets. *Solid Earth*, (5):1047–1070.
- 461 Hunstad, I. and England, P. (1999). An upper bound on the rate of strain in the central
462 apennines, italy, from triangulation measurements between 1869 and 1963. *Earth and*
463 *Planetary Science Letters*, 169(3-4):261–267.
- 464 Igarashi, T. (2010). Spatial changes of inter-plate coupling inferred from sequences of small
465 repeating earthquakes in japan. *Geophysical research letters*, 37(20).
- 466 Igarashi, T., Matsuzawa, T., and Hasegawa, A. (2003). Repeating earthquakes and inter-
467 plate aseismic slip in the northeastern japan subduction zone. *Journal of Geophysical*
468 *Research: Solid Earth*, 108(B5).
- 469 Inbal, A., Ampuero, J.-P., and Avouac, J.-P. (2017). Locally and remotely triggered aseismic
470 slip on the central San Jacinto fault near Anza, ca, from joint inversion of seismicity and
471 strainmeter data. *Journal of Geophysical Research: Solid Earth*, 122(4):3033–3061.

- 472 Jones, L. M. and Molnar, P. (1979). Some characteristics of foreshocks and their pos-
473 sible relationship to earthquake prediction and premonitory slip on faults. *Journal of*
474 *Geophysical Research: Solid Earth*, 84(B7):3596–3608.
- 475 Jones, L. M. (1985). Foreshocks and time-dependent earthquake hazard assessment in
476 southern california. *Bulletin of the Seismological Society of America*, 75(6):1669–1679.
- 477 Kagan, Y. and Jackson, D. D. (1991). Long-term earthquake clustering. *Geophysical Journal*
478 *International*, 104(1):117–133.
- 479 Kagan, Y. and Knopoff, L. (1978). Statistical study of the occurrence of shallow earth-
480 quakes. *Geophysical Journal International*, 55(1):67–86.
- 481 Kato, A., Obara, K., Igarashi, T., Tsuruoka, H., Nakagawa, S., and Hirata, N. (2012).
482 Propagation of slow slip leading up to the 2011 mw 9.0 tohoku-oki earthquake. *Science*,
483 335(6069):705–708.
- 484 Liu, Y. and Rice, J. R. (2005). Aseismic slip transients emerge spontaneously in three-
485 dimensional rate and state modeling of subduction earthquake sequences. *Journal of*
486 *Geophysical Research: Solid Earth*, 110(B8).
- 487 Malin, P. E., Bohnhoff, M., Blümle, F., Dresen, G., Martínez-Garzón, P., Nurlu, M., Ceken,
488 U., Kadiriloglu, F. T., Kartal, R. F., Kilic, T., et al. (2018). Microearthquakes preceding
489 a m4. 2 earthquake offshore istanbul. *Scientific reports*, 8(1):1–11.
- 490 Marone, C. (1998). The effect of loading rate on static friction and the rate of fault healing
491 during the earthquake cycle. *Nature*, 391(6662):69–72.
- 492 McLaskey, G. C. (2019). Earthquake initiation from laboratory observations and implica-
493 tions for foreshocks. *Journal of Geophysical Research: Solid Earth*.

494 McMahon, N. D., Aster, R. C., Yeck, W. L., McNamara, D. E., and Benz, H. M. (2017).
495 Spatiotemporal evolution of the 2011 prague, oklahoma, aftershock sequence revealed
496 using subspace detection and relocation. *Geophysical Research Letters*, 44(14):7149–7158.

497 McMahon, N. D., Yeck, W. L., Stickney, M. C., Aster, R. C., Martens, H. R., and Benz,
498 H. M. (2019). Spatiotemporal analysis of the foreshock–mainshock–aftershock sequence
499 of the 6 july 2017 m w 5.8 lincoln, montana, earthquake. *Seismological Research Letters*,
500 90(1):131–139.

501 Mignan, A. (2014). The debate on the prognostic value of earthquake foreshocks: A meta-
502 analysis. *Scientific reports*, 4:4099.

503 Mogi, K. (1963). Some discussions on aftershocks, foreshocks and earthquake swarms:
504 the fracture of a semi-infinite body caused by an inner stress origin and its relation to
505 the earthquake phenomena (third paper). *Bulletin of the Earthquake Research Institute*,
506 *University of Tokyo*, 41(3):615–658.

507 Molchanov, O., Hayakawa, M., Oudoh, T., and Kawai, E. (1998). Precursory effects in the
508 subionospheric vlf signals for the kobe earthquake. *Physics of the Earth and Planetary*
509 *Interiors*, 105(3-4):239–248.

510 Nadeau, R. M. and McEvilly, T. V. (1999). Fault slip rates at depth from recurrence
511 intervals of repeating microearthquakes. *Science*, 285(5428):718–721.

512 Papazachos, B. (1975). Foreshocks and earthquake prediction. *Tectonophysics*, 28(4):213–
513 226.

514 Pedregosa, F., Varoquaux, G., Gramfort, A., Michel, V., Thirion, B., Grisel, O., Blondel,
515 M., Prettenhofer, P., Weiss, R., Dubourg, V., Vanderplas, J., Passos, A., Cournapeau,
516 D., Brucher, M., Perrot, M., and Duchesnay, E. (2011). Scikit-learn: Machine learning
517 in Python. *Journal of Machine Learning Research*, 12:2825–2830.

518 Poli, P., Marguin, V., Wang, Q., Dagostino, N., and Johnson, P. (2020a). Seasonal and co-
519 seismic velocity variation in the region of laquila from single station measurements and
520 implications for crustal rheology. *Journal of Geophysical Research: Solid Earth*, page
521 e2019JB019316.

522 Poli, P., Soaga, J., Molinari, I., Cascone, V., and Boschi, L. (2020b). The 2020 coronavirus
523 lockdown and seismic monitoring of anthropic activities in northern italy. *Sci Rep*, 10:–.

524 Reasenberg, P. A. (1999). Foreshock occurrence before large earthquakes. *Journal of*
525 *Geophysical Research: Solid Earth*, 104(B3):4755–4768.

526 Renard, F., McBeck, J., Kandula, N., Cordonnier, B., Meakin, P., and Ben-Zion, Y. (2019).
527 Volumetric and shear processes in crystalline rock approaching faulting. *Proceedings of*
528 *the National Academy of Sciences*, 116(33):16234–16239.

529 Rikitake, T. (1975). Earthquake precursors. *Bulletin of the Seismological Society of Amer-*
530 *ica*, 65(5):1133–1162.

531 Roberts, G. P. and Michetti, A. M. (2004). Spatial and temporal variations in growth rates
532 along active normal fault systems: an example from the lazio–abruzzo apennines, central
533 italy. *Journal of Structural Geology*, 26(2):339–376.

534 Ross, Z. E., Rollins, C., Cochran, E. S., Hauksson, E., Avouac, J.-P., and Ben-Zion, Y.
535 (2017). Aftershocks driven by afterslip and fluid pressure sweeping through a fault-
536 fracture mesh. *Geophysical Research Letters*, 44(16):8260–8267.

537 Rubin, A. M. and Ampuero, J.-P. (2005). Earthquake nucleation on (aging) rate and state
538 faults. *Journal of Geophysical Research: Solid Earth*, 110(B11).

539 Ruiz, S., Aden-Antoniow, F., Baez, J., Otarola, C., Potin, B., del Campo, F., Poli, P.,
540 Flores, C., Satriano, C., Leyton, F., et al. (2017). Nucleation phase and dynamic inversion

541 of the mw 6.9 valparaíso 2017 earthquake in central chile. *Geophysical Research Letters*,
542 44(20):10–290.

543 Ruiz, S., Metois, M., Fuenzalida, A., Ruiz, J., Leyton, F., Grandin, R., Vigny, C.,
544 Madariaga, R., and Campos, J. (2014a). Intense foreshocks and a slow slip event preceded
545 the 2014 iquique mw 8.1 earthquake. *Science*, 345(6201):1165–1169.

546 Ruiz, S., Metois, M., Fuenzalida, A., Ruiz, J., Leyton, F., Grandin, R., Vigny, C.,
547 Madariaga, R., and Campos, J. (2014b). Intense foreshocks and a slow slip event preceded
548 the 2014 iquique mw 8.1 earthquake. *Science*, 345(6201):1165–1169.

549 Savage, H. M., Keranen, K. M., P. Schaff, D., and Dieck, C. (2017). Possible precursory
550 signals in damage zone foreshocks. *Geophysical Research Letters*, 44(11):5411–5417.

551 Schoenball, M. and Ellsworth, W. L. (2017). A systematic assessment of the spatiotemporal
552 evolution of fault activation through induced seismicity in oklahoma and southern kansas.
553 *Journal of Geophysical Research: Solid Earth*, 122(12):10–189.

554 Schurr, B., Asch, G., Hainzl, S., Bedford, J., Hoechner, A., Palo, M., Wang, R., Moreno,
555 M., Bartsch, M., Zhang, Y., et al. (2014). Gradual unlocking of plate boundary controlled
556 initiation of the 2014 iquique earthquake. *Nature*, 512(7514):299–302.

557 Shelly, D. R., Beroza, G. C., and Ide, S. (2007). Complex evolution of transient slip de-
558 rived from precise tremor locations in western shikoku, japan. *Geochemistry, Geophysics,*
559 *Geosystems*, 8(10).

560 Shelly, D. R. and Hardebeck, J. L. (2019). Illuminating faulting complexity of the 2017
561 yellowstone maple creek earthquake swarm. *Geophysical Research Letters*, 46(5):2544–
562 2552.

563 Shen, Z.-K., Jackson, D. D., Feng, Y., Cline, M., Kim, M., Fang, P., and Bock, Y. (1994).

564 Postseismic deformation following the landers earthquake, california, 28 june 1992. *Bul-*
565 *letin of the Seismological Society of America*, 84(3):780–791.

566 Singh, R. P., Mehdi, W., Gautam, R., Senthil Kumar, J., Zlotnicki, J., and Kafatos, M.
567 (2010). Precursory signals using satellite and ground data associated with the wenchuan
568 earthquake of 12 may 2008. *International Journal of Remote Sensing*, 31(13):3341–3354.

569 Stein, R. S. and Lisowski, M. (1983). The 1979 homestead valley earthquake sequence,
570 california: Control of aftershocks and postseismic deformation. *Journal of Geophysical*
571 *Research: Solid Earth*, 88(B8):6477–6490.

572 Tape, C., Holtkamp, S., Silwal, V., Hawthorne, J., Kaneko, Y., Ampuero, J. P., Ji, C.,
573 Ruppert, N., Smith, K., and West, M. E. (2018). Earthquake nucleation and fault slip
574 complexity in the lower crust of central alaska. *Nature Geoscience*, 11(7):536–541.

575 Toda, S., Stein, R. S., Sevilgen, V., and Lin, J. (2011). Coulomb 3.3 graphic-rich defor-
576 mation and stress-change software for earthquake, tectonic, and volcano research and
577 teachinguser guide. *US Geological Survey open-file report*, 1060(2011):63.

578 Tramutoli, V., Corrado, R., Filizzola, C., Genzano, N., Lisi, M., and Pergola, N. (2015).
579 From visual comparison to robust satellite techniques: 30 years of thermal infrared satel-
580 lite data analyses for the study of earthquake preparation phases. *Bollettino di Geofisica*
581 *Teorica ed Applicata*, 56(2).

582 Trugman, D. T., Ross, Z. E., and Johnson, P. A. (2020). Imaging stress and fault-
583 ing complexity through earthquake waveform similarity. *Geophysical Research Letters*,
584 47(1):e2019GL085888.

585 Uchida, N. (2019). Detection of repeating earthquakes and their application in character-
586 izing slow fault slip. *Progress in Earth and Planetary Science*, 6(1):40.

- 587 Uchida, N. and Bürgmann, R. (2019). Repeating earthquakes. *Annual Review of Earth and*
588 *Planetary Sciences*, 47:305–332.
- 589 Virk, H. and Walia, V. (2001). Helium/radon precursory signals of chamoli earthquake,
590 india. *Radiation measurements*, 34(1-6):379–384.
- 591 Waldhauser, F. (2001). hypodda program to compute double-difference hypocenter loca-
592 tions (hypodd version 1.0-03/2001). *US Geol. Surv. Open File Rep.*, 01, 113.
- 593 Ward Jr, J. H. (1963). Hierarchical grouping to optimize an objective function. *Journal of*
594 *the American statistical association*, 58(301):236–244.
- 595 Wedmore, L., Walker, J. F., Roberts, G. P., Sammonds, P., McCaffrey, K., and Cowie, P.
596 (2017). A 667 year record of coseismic and interseismic coulomb stress changes in central
597 italy reveals the role of fault interaction in controlling irregular earthquake recurrence
598 intervals. *Journal of Geophysical Research: Solid Earth*, 122(7):5691–5711.
- 599 Wehling-Benatelli, S., Becker, D., Bischoff, M., Friederich, W., and Meier, T. (2013). In-
600 dications for different types of brittle failure due to active coal mining using waveform
601 similarities of induced seismic events. *Solid Earth*, 4(2).
- 602 Wessel, P., Luis, J., Uieda, L., Scharroo, R., Wobbe, F., Smith, W., and Tian, D.
603 (2019). The generic mapping tools version 6. *Geochemistry, Geophysics, Geosystems*,
604 20(11):5556–5564.
- 605 Westaway, R. (1992). Seismic moment summation for historical earthquakes in italy: tec-
606 tonic implications. *Journal of Geophysical Research: Solid Earth*, 97(B11):15437–15464.
- 607 Yoon, C. E., Yoshimitsu, N., Ellsworth, W. L., and Beroza, G. C. (2019). Foreshocks and
608 mainshock nucleation of the 1999 m w 7.1 hector mine, california, earthquake. *Journal*
609 *of Geophysical Research: Solid Earth*, 124(2):1569–1582.

610 Zang, A., Christian Wagner, F., Stanchits, S., Dresen, G., Andresen, R., and Haidekker,
611 M. A. (1998). Source analysis of acoustic emissions in aue granite cores under symmetric
612 and asymmetric compressive loads. *Geophysical Journal International*, 135(3):1113–1130.

613 Zhao, L.-S. and Helmberger, D. V. (1994). Source estimation from broadband regional
614 seismograms. *Bulletin of the Seismological Society of America*, 84(1):91–104.

615 Zhu, L. and Helmberger, D. V. (1996). Advancement in source estimation techniques
616 using broadband regional seismograms. *Bulletin of the Seismological Society of America*,
617 86(5):1634–1641.

618 **Authors mailing list**

Hugo S. Sánchez-Reyes hugo.sanchez-reyes@univ-grenoble-alpes.fr
ISTerre, Université Grenoble Alpes
CS 40700, 38058 Grenoble Cedex 9, France

David Essing david.essing@univ-grenoble-alpes.fr
ISTerre, Université Grenoble Alpes
CS 40700, 38058 Grenoble Cedex 9, France

Eric Beaucé ebeauce@mit.edu
Dept. of Earth, Atmospheric and Planetary Sciences
Massachusetts Institute of Technology,
77 Massachusetts Avenue, 54-527,
Cambridge, MA 02139-4307, USA

Piero Poli piero.poli@univ-grenoble-alpes.fr
ISTerre, Université Grenoble Alpes
CS 40700, 38058 Grenoble Cedex 9, France

619 Figure Captions

Figure 1. Regional map of the study area. The yellow square inside the small map inset on the left corresponds to the central region of Italy represented in the larger topographic map. The small map inset on the right represents magnification of the black dashed area around the epicentral location (red star). The color code used in the map view on the right represents the estimated depth of the foreshock and aftershock activity (estimated in this study: 714 events). The yellow circle represents Balsorano city, and the white triangles represent the stations used in this study. The dashed lines in the right inset map represent the directions A-A' (along strike) and B-B' (normal to the strike) illustrated in the cross sections of Figure 5. The solid red line represents the superficial scarp of the Liri fault (scarp taken from [Wedmore et al. \(2017\)](#)).

Figure 2. (a) Spectrogram on VVLD.HHZ. The white line is the median of the energy in the frequency band between 5 Hz and 20 Hz calculated within a 1-h sliding window. Notice the diurnal energy variation. (b) Blue, cumulative events for the same time period of the experiment; orange, recurrence time for the newly detected events. (c) Estimated magnitudes for the newly detected events. For illustration purposes, the estimated lowest magnitude shown in (c) is 0. A gap in the continuous data at this receiver location is seen for the night of November 8 to 9, 2019. In all panels, night periods (18:00 to 6:00) are represented by shaded regions.

Figure 3. Illustration of the waveform-based hierarchical clustering output. (a) Pairwise correlation coefficients between the waveforms for the vertical component of station VVLD (Fig. 1) of the 714 detected events. This matrix is used to perform the hierarchical clustering. (b) Cumulative events combined with the results from the hierarchical clustering,

according to the color code in the legend. (c) Characteristic normalized waveforms (vertical component) of the five different clusters revealed in the earthquake sequence. These traces are obtained after stacking all of the individually normalized waveforms belonging to each cluster.

Figure 4. Spatio-temporal evolution of the earthquake sequences with respect to the mainshock origin time and hypocenter. Left column: Temporal density (number of events per hour). The coefficients of variation (COV) from the recurrence times are indicated for each cluster. Center column: Distance in time and space from each event of the sequence with respect to the mainshock location and origin time. The dashed gray line on the left and center column represents the mainshock origin time. Right column: Spatial density (concentration of events per 0.1 km). Dashed black line, where 90% of the seismic activity is concentrated. (a)-(e) Each of the five clusters progressively ordered. The same color code from Figure 3 is used.

Figure 5. Map view (left column), and cross-sections along the strike (middle column) and normal-strike (right column) directions for each of the five clusters identified in the sequence (as indicated). All of the locations are relative to the mainshock hypocenter (41.7746°N 13.6066°E ; 13.94 km depth, black star). In all of the panels, the same color code is used as in Figures 3 and 4 to represent each different cluster. The solid black line represents a fault plane of 1 km^2 with the geometry of the second nodal plane (Supplementary Materials Table S1). The directions A-A' (along strike) and B-B' (normal to the strike) are the same as in Figure 1. Each cluster is represented by a corresponding label a) Cluster 1, b) Cluster 2, c) Cluster 3, d) Cluster 4 and e) Cluster 5. In each panel, the black circles represent the location of the templates belonging to each cluster.

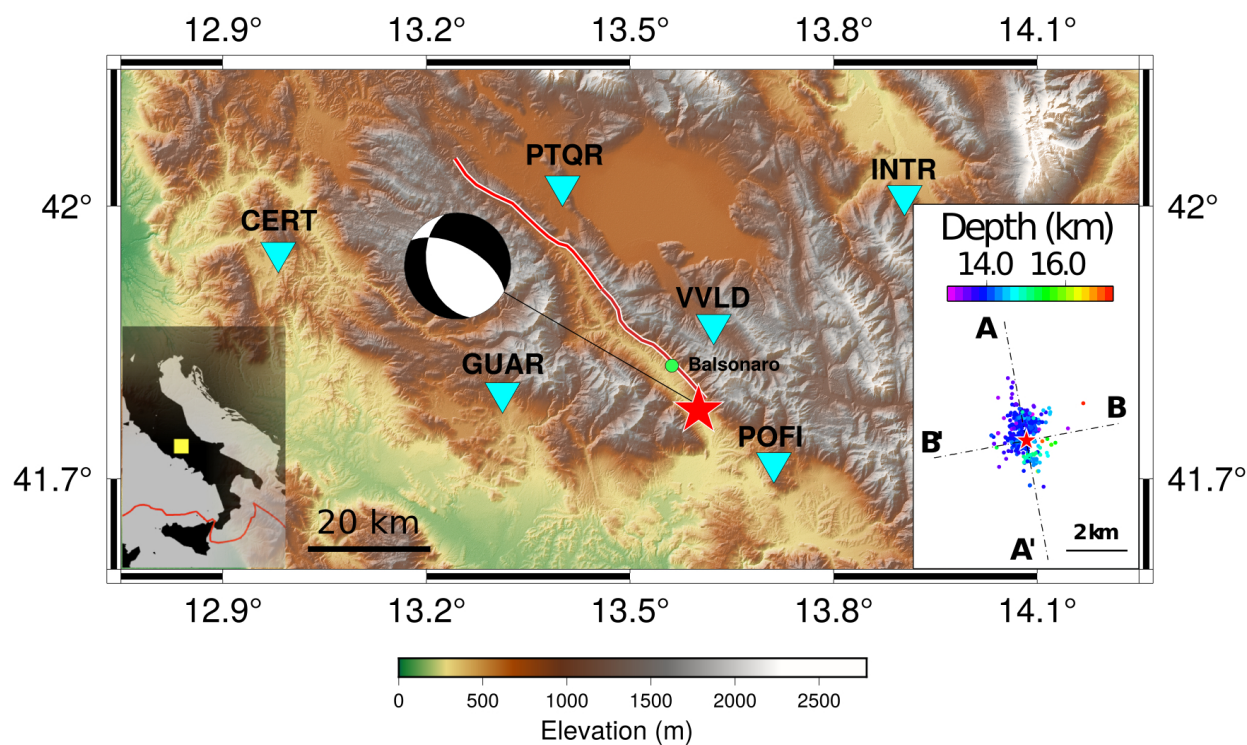


Figure 1: Regional map of the study area. The yellow square inside the small map inset on the left corresponds to the central region of Italy represented in the larger topographic map. The small map inset on the right represents magnification of the black dashed area around the epicentral location (red star). The color code used in the map view on the right represents the estimated depth of the foreshock and aftershock activity (estimated in this study: 714 events). The yellow circle represents Balsorano city, and the white triangles represent the stations used in this study. The dashed lines in the right inset map represent the directions A-A' (along strike) and B-B' (normal to the strike) illustrated in the cross sections of Figure 5. The solid red line represents the superficial scarp of the Liri fault (scarp taken from [Wedmore et al. \(2017\)](#)).

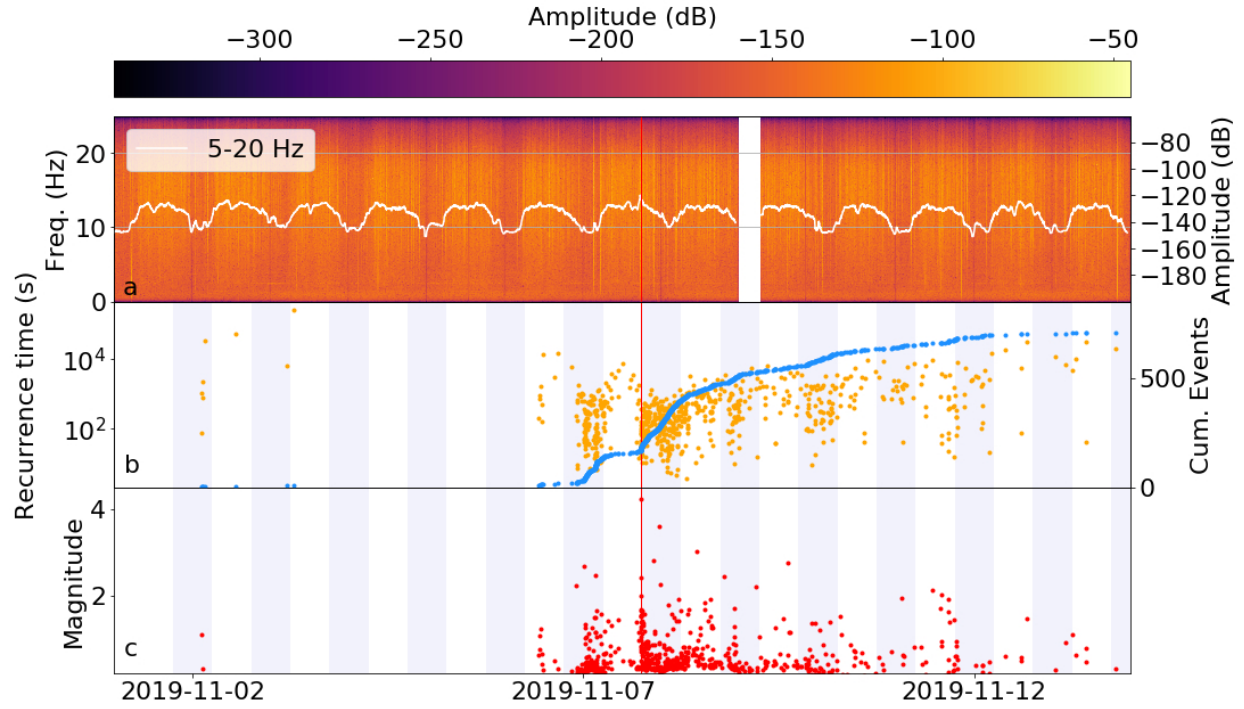


Figure 2: (a) Spectrogram on VVLD.HHZ. The white line is the median of the energy in the frequency band between 5 Hz and 20 Hz calculated within a 1-h sliding window. Notice the diurnal energy variation. (b) Blue, cumulative events for the same time period of the experiment; orange, recurrence time for the newly detected events. (c) Estimated magnitudes for the newly detected events. For illustration purposes, the estimated lowest magnitude shown in (c) is 0. A gap in the continuous data at this receiver location is seen for the night of November 8 to 9, 2019. In all panels, night periods (18:00 to 6:00) are represented by shaded regions.

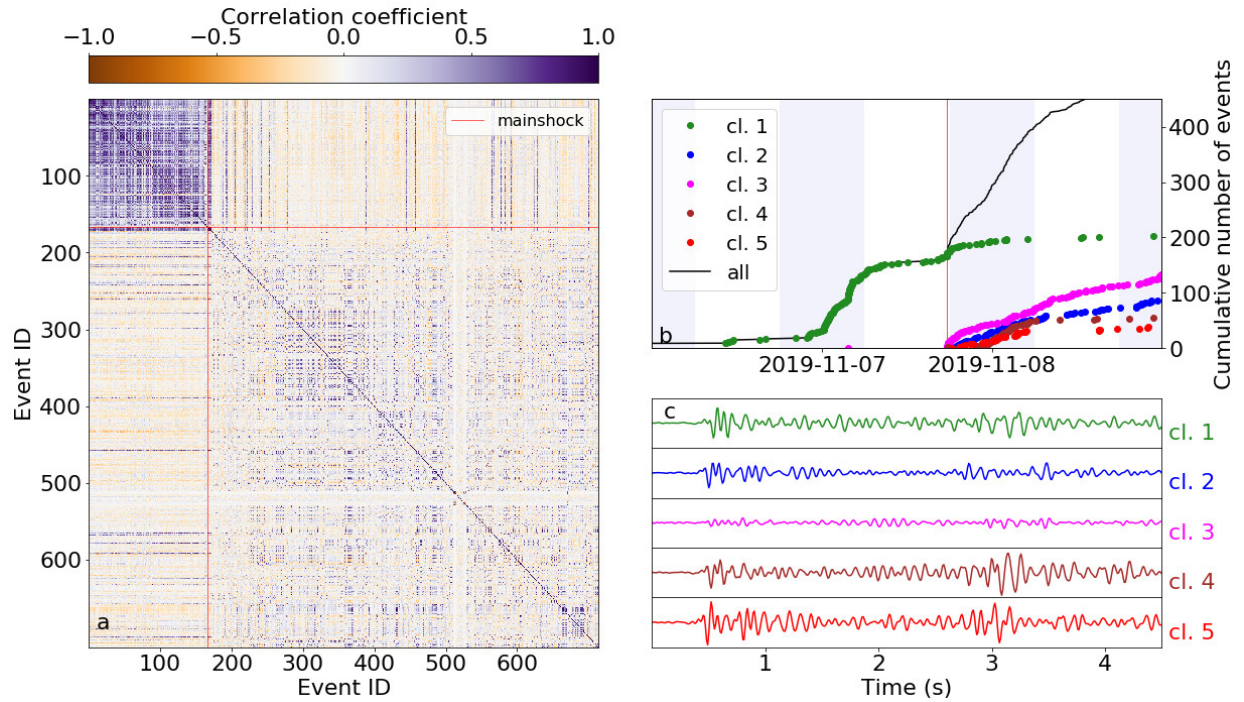


Figure 3: Illustration of the waveform-based hierarchical clustering output. (a) Pairwise correlation coefficients between the waveforms for the vertical component of station VVLD (Fig. 1) of the 714 detected events. This matrix is used to perform the hierarchical clustering. (b) Cumulative events combined with the results from the hierarchical clustering, according to the color code in the legend. (c) Characteristic normalized waveforms (vertical component) of the five different clusters revealed in the earthquake sequence. These traces are obtained after stacking all of the individually normalized waveforms belonging to each cluster.

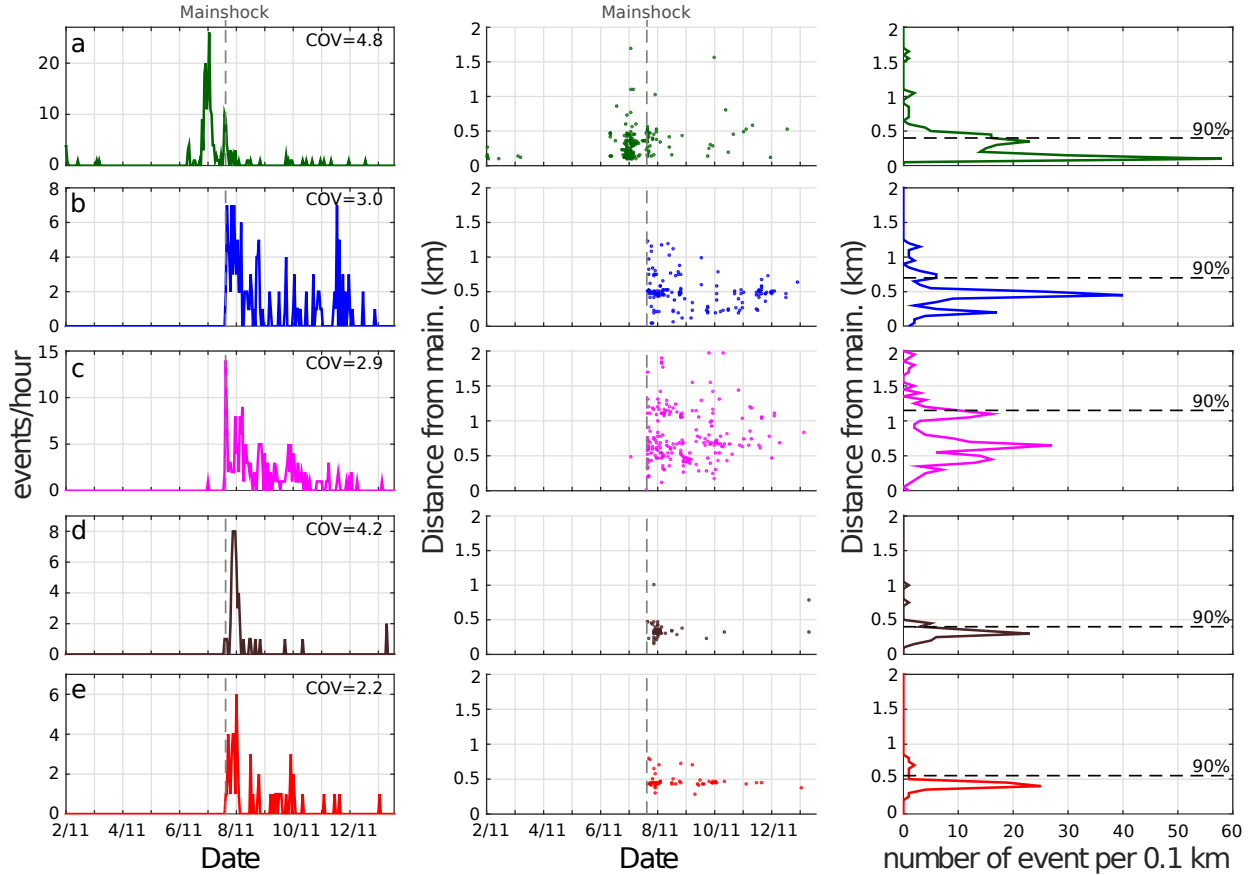


Figure 4: Spatio-temporal evolution of the earthquake sequences with respect to the mainshock origin time and hypocenter. Left column: Temporal density (number of events per hour). The coefficients of variation (COV) from the recurrence times are indicated for each cluster. Center column: Distance in time and space from each event of the sequence with respect to the mainshock location and origin time. The dashed gray line on the left and center column represents the mainshock origin time. Right column: Spatial density (concentration of events per 0.1 km). Dashed black line, where 90% of the seismic activity is concentrated. (a)-(e) Each of the five clusters progressively ordered. The same color code from Figure 3 is used.

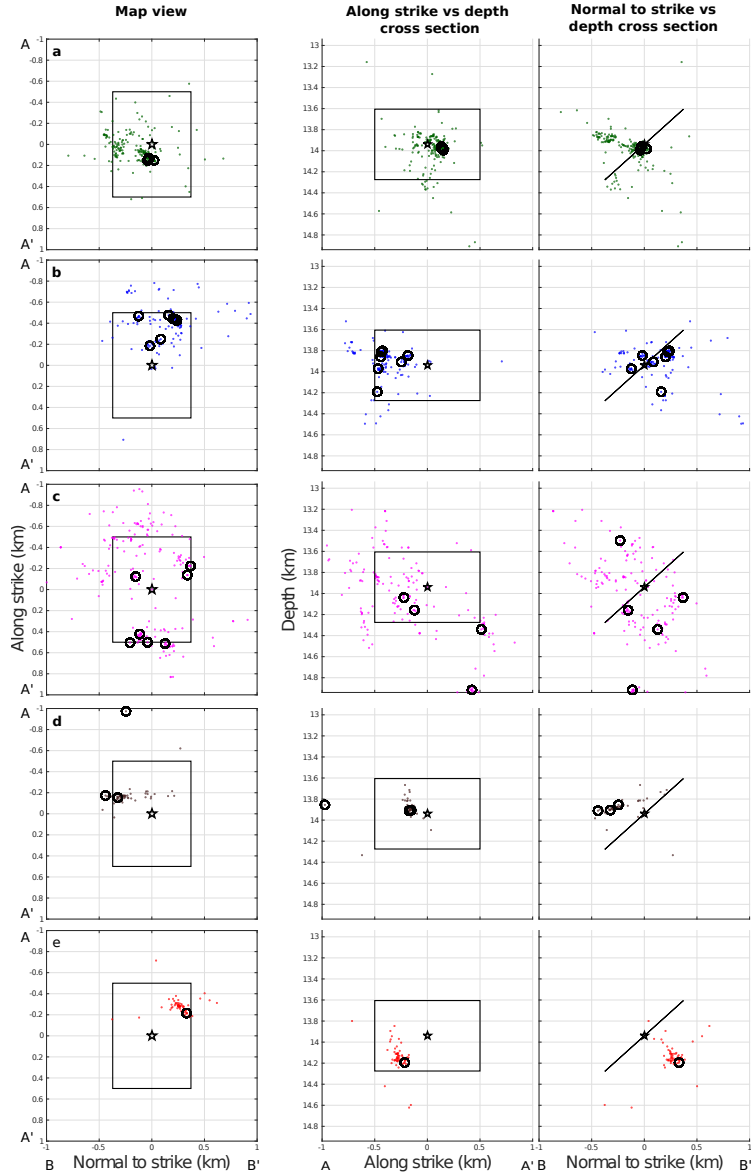


Figure 5: Map view (left column), and cross-sections along the strike (middle column) and normal-strike (right column) directions for each of the five clusters identified in the sequence (as indicated). All of the locations are relative to the mainshock hypocenter (41.7746°N 13.6066°E ; 13.94 km depth, black star). In all of the panels, the same color code is used as in Figures 3 and 4 to represent each different cluster. The solid black line represents a fault plane of 1 km^2 with the geometry of the second nodal plane (Supplementary Materials Table S1). The directions A-A' (along strike) and B-B' (normal to the strike) are the same as in Figure 1. Each cluster is represented by a corresponding label a) Cluster 1, b) Cluster 2, c) Cluster 3, d) Cluster 4 and e) Cluster 5. In each panel, the black circles represent the location of the templates belonging to each cluster.